BRIEF COMMUNICATION   **OPEN**

Check for updates

Study on the corrosion behavior of NiTi shape memory alloys fabricated by electron beam melting

Lianmin Zhang[1,4], Dechun Ren[2,4], Haibin Ji[2✉], Aili Ma[1], Enobong Felix Daniel[3], Shujun Li[2], Wei Jin[2] and Yugui Zheng[1✉]

The poor processability of NiTi shape memory alloy with superior resistance to corrosion and wear is an important reason for hindering its extensive application. In this work, NiTi alloy was fabricated by electron beam melting (EBM) using different fabrication parameters including changed speed function and focus offset. Furthermore, the influence of these parameters on the corrosion behavior of EBM NiTi alloys was investigated. It was found that the variation in fabrication parameters caused different defect types and defect number, thus affecting the corrosion resistance of NiTi alloys. The alloy with a large number of cracks displayed the lowest corrosion resistance, while a superior corrosion resistance equivalent to the wrought alloy was observed when a few small pores were uniformly distributed in the alloys. Electrochemical results indicated that the EBM NiTi alloy with optimized fabrication parameters presented a low carrier density indicating good protective ability of the passive films.

npj Materials Degradation (2022)6:79 ; https://doi.org/10.1038/s41529-022-00289-3

INTRODUCTION

NiTi alloy with a near equal atomic ratio is often used in aerospace, communication, naval ships, and medical devices due to its good shape memory effect or super-elasticity, high wear-resistant performance and superior corrosion resistance[1–5]. It is mainly composed of high-temperature austenite (B2) and low-temperature martensite (B19′), which endow it with the shape memory effect by the solid-state transformation between the two phases[1,4,5]. However, the poor processability of NiTi alloy substantially restrict its extensive application[6,7]. Therefore, it is necessary to seek a reliable preparation method for NiTi alloy.

Additive manufacturing, commonly known as 3D printing, is a kind of near-net forming technology, which uses computer-aided system to discretize the three-dimensional structure of components into two-dimensional data model, and uses the method of limiting the accumulation of raw materials and the melting path of heat source to realize the layer-by-layer accumulation of components[8–12]. In order to solve the difficult machining problem of NiTi alloy, additive manufacturing can be adopted to create integral formation of complex components. At present, the most widely used additive manufacturing technologies are selective laser melting (SLM) and electron beam melting (EBM)[13–15]. The corrosion behavior of SLM Ti–6Al–4V alloy was studied by Dai et al. and they found that the corrosion resistance of the alloy was significantly lower than that of traditionally processed Grade 5 alloy, and this was mainly attributed to a large amount of acicular α′ phase and a small amount of β-Ti phase[15]. Furthermore, by increasing the heat treatment temperature, the metastable acicular α′ phase was eliminated, and the plate-like α phase and the lamella α + β in the SLM Ti–6Al–4V alloy was obtained. However, a decrease in corrosion resistance was recorded due to the increased grain size with the elevated heat treatment temperature[13]. In addition, it was reported that the Ti–5Cu alloy prepared by SLM had many inhomogeneous Ti₂Cu phases and there also existed some α′ phases containing rare-earth elements

at the boundary of the molten pool, which led to the decrease in corrosion resistance[16]. Compared with the SLM alloys, the EBM materials are usually prepared in a high vacuum environment, which can effectively prevent the introduction of O, N, and other impurity elements[17]. Meanwhile, EBM has the preheating of the fabricating substrate and the powder, and the preheating can significantly reduce the internal defects and the residual thermal stress of samples, thereby improving the mechanical properties and corrosion resistance[18–21]. Some researchers reported that the Ti–6Al–4V alloy produced by EBM had higher corrosion resistance compared with the wrought Ti–6Al–4V alloy, and they attributed it to the higher fraction of β phase and the remarkably refined lamellar α + β phases[20,21]. Gai et al. monitored the change of electrochemical corrosion behavior with the pore depth of a porous Ti–6Al–4V alloy fabricated by EBM in situ, and found that the deep pore position of the EBM sample demonstrated superior corrosion resistance[18]. However, to the best of our knowledge, the corrosion behavior of NiTi alloy prepared by EBM has not been reported.

The corrosion resistance of NiTi alloy made by EBM should be closely related to the internal defects including pores and cracks[22,23]. By adjusting the fabrication parameters, the internal structural defects of alloys can be optimized to improve their corrosion resistance. Among the EBM fabrication parameters, focus offset (FO) and speed function (SF) are two key parameters. During the fabrication process of EBM, some important fabrication parameters such as the transverse displacement rate of electron beam cannot be directly changed, but they can be indirectly controlled by adjusting the parameters of FO and SF[24–26]. With regard to FO, it is the additional current generated by the electromagnetic coil, which is the offset of the electron beam from the zero position of the focusing plane and controls the volume of the molten pool[24,27]. Changing the value of FO is a convenient way to adjust the type and number of internal defects[27]. With respect to SF, it is an index representing the relationship between the scanning rate of electron beam and the current on focusing

plane, by which the molten pool depth can be kept relatively constant during the whole fabricating process regardless of the change in electron beam current. That is to say, when the electron beam current increases, the scanning rate of the electron beam increases accordingly to offset the influence of the change in electron beam power[28]. With other parameters fixed, the increase of FO will lead to an increase in spot size and a decrease in energy density. When the electron beam current is determined, the scanning rate of the electron beam increases and the energy density decreases with the increase of SF[24]. Therefore, the changes of FO and SF can significantly affect the defects in NiTi alloy fabricated by EBM, and further influence the corrosion behavior of NiTi alloy. Up to now, there is no systematic research on the influence of fabrication parameters on the corrosion behavior of EBM NiTi alloy.

Herein, the NiTi alloy samples were fabricated by EBM with variation in FO and SF. The phase composition and surface morphology of EBM NiTi alloys were characterized by X-ray diffraction (XRD) and scanning electron microscopy. The type and distribution of defects in different NiTi alloys were detected using X-ray micro-tomography system. The corrosion behavior of EBM samples with different fabrication parameters was evaluated by electrochemical impedance, potentiodynamic polarization, and Mott–Schottky techniques, and the influence of pores and cracks on the corrosion resistance of EBM NiTi alloys was discussed in detail. This research provides some important insights for the preparation of NiTi alloy with superior corrosion resistance by EBM.

RESULTS AND DISCUSSION

Microstructure and phase composition of NiTi alloys

Figure 1a shows the morphology of NiTi powders selected for EBM. As observed, the morphology of powders is spherical with relatively smooth surfaces, although a few small satellite powders are adhered to the surface. The size distribution of the powder as shown in Fig. 1b ranges from 53 to 106 μm. The average diameter (D_{50}) of the powder is about 62.48 μm. With the cumulative volume percent distribution of powder reaching 10% (D_{10}) and 90% (D_{90}), the corresponding diameters are 45.18 μm and 82.17 μm, respectively. It should be noted that the powder with this size range showed superior fabricating performance of titanium alloy in previous research[17]. XRD results demonstrate that the alloy powder is mainly composed of B19′ and $NiTi_2$ phases (Fig. 1c), and the DSC curve of the powder is presented in Supplementary Fig. 1. Furthermore, seven kinds of NiTi alloys are prepared by adjusting different EBM fabrication parameters using the alloy powder, and the XRD results of different EBM NiTi alloys are shown in Fig. 1d. Obviously, the phase composition of the different NiTi alloys with changed FO and SF remains consistent, and all samples only contain B19′ phase and $NiTi_2$ phase, which is consistent with the used NiTi alloy powder. It should be noted that the testing plane for XRD is the building direction plane, and no obvious B2 phase is recorded probably due to its low content, therefore displaying a different result compared with the result perpendicular to the building plane which has some small B2 peaks. Since the phase composition of all samples is the same, a representative image of scanning electron microscope (SEM) for S5 is shown in Fig. 1e (the detailed surface morphologies perpendicular and parallel to the building direction of S1, S5 and S7 are displayed in Supplementary Fig. 2 to Supplementary Fig. 6). It can be seen that there are two different phases with significant color differences, where the black dot corresponds to the $NiTi_2$ phase and the other represents the B19′ phase based on the analysis of XRD. Furthermore, the microstructure of S5 is characterized by transmission electron microscope (TEM), as displayed in Fig. 1f. The results of bright-field image show obvious

lath distribution and a large number of dislocations between the laths are recorded. The selected area electron diffraction (inset diagram in Fig. 1f) indicates that these bright laths are B19′ twins, which are similar to the microstructure of the traditional wrought NiTi alloy[29].

Defect analysis of different EBM NiTi alloys

Pores and cracks are two kinds of key defects weakening the corrosion resistance as well as the mechanical properties of materials. In order to analyze the influence of different fabrication parameters on the defects of EBM NiTi alloys, S5, S7 and S1 were selected for the defect analysis since these three kinds of samples have the maximum, the medium and the minimum compressive strength and compressive plasticity, respectively, according to the test results shown in Supplementary Fig. 7. Figure 2a–c shows the three-dimensional X-ray tomography (XRT) of S1, S5 and S7, respectively. Since the different absorption ability of X-ray by the pores/cracks and the alloy, black points and lines correspond to pores and cracks, respectively, based on relevant analysis, while the gray area indicates the NiTi alloy with dense structure. It is observed that the main defect of S1 is through cracks, and a few scattered pores distributed on the surface are detected. In regard of S5, the main defects are pores and no cracks are observed. For S7, cracks and pores are all observed on the alloy surface, however, the crack length is shorter compared with that in S1. Furthermore, the three-dimensional distribution of pores and cracks in the three kinds of samples is presented in Fig. 2d–f. For S1 and S7, obvious cracks (pink and yellow areas) are recorded. The cracks in S1 are relatively straight and continuous, which seems that they can directly cut the sample into different parts. In contrast, the cracks in S7 are short and only locally cut the sample. However, S5 is completely different from the above two samples. There are some small pores uniformly distributed in the sample without cracks. The results of defect analysis indicate that S5 has the least defects, followed by S7 and S1. The main reason for the formation of pores in the EBM NiTi alloy may be related to the protective inert gas in the powders after the gas atomization preparation. At the same time, the unmelted powder due to insufficient energy input or the poor bonding between the melted layers can also play an important role in the formation of pores. For the generation of cracks, the following reasons are viable; firstly, the material in the melting pool and in the boundary area of the melting pool may be limited by the material in the low-temperature area during the fabricating process, causing compressive stress. Meanwhile, the yield strength of the material in the heated area will decrease due to the rising temperature, and the material will be in the plastic thermal compression state when the compressive stress is larger than the reduced yield strength. Also, the material will be constrained by the cooling shrinkage of the surrounding material as it cools. At this time, residual stress will appear in the cladding layer, and cracks will occur when the residual stress exceeds the strength limit of the material[30]. It is worth noting that the changes in FO and SF have significant effects on the formation of defects in EBM NiTi alloy. Concerning FO, it is the additional current generated by the electromagnetic coil that can control the volume of the molten pool to some extent[24,27]. With other parameters fixed, the increase of FO will lead to the increase in spot size and the decrease in energy density[27]. That is, a large FO usually means an insufficient energy density resulting in the poor powder melting effect, and a very small FO may cause volatilization or burning loss of alloy components. In retrospect, S5 has a suitable value of FO just showing fewer defects, while S1 has a small FO value displaying more defects, especially cracks. With respect to SF, it is an index representing the relationship between the scanning rate of electron beam and the current on focusing plane, by which the molten pool depth can be kept relatively constant during the
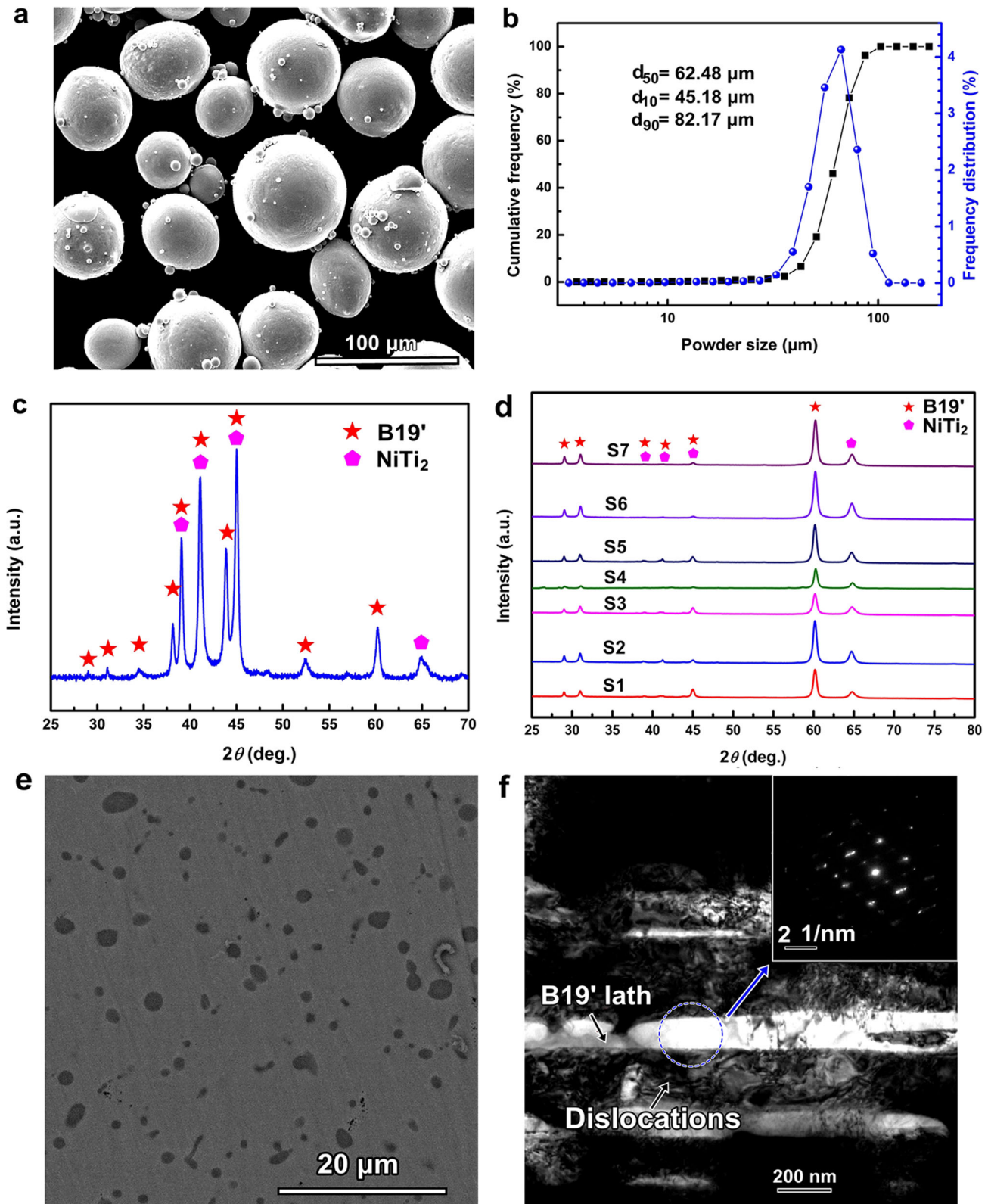
Fig. 1 Microstructure and phase composition of NiTi powders and EBM NiTi alloys. a SEM morphology, **b** size distribution, and **c** XRD phase composition of NiTi alloy powder; **d** XRD phase composition of different EBM NiTi alloys, **e** backscattered electron image of S5, **f** TEM bright field image of S5 (the inset is SAED).
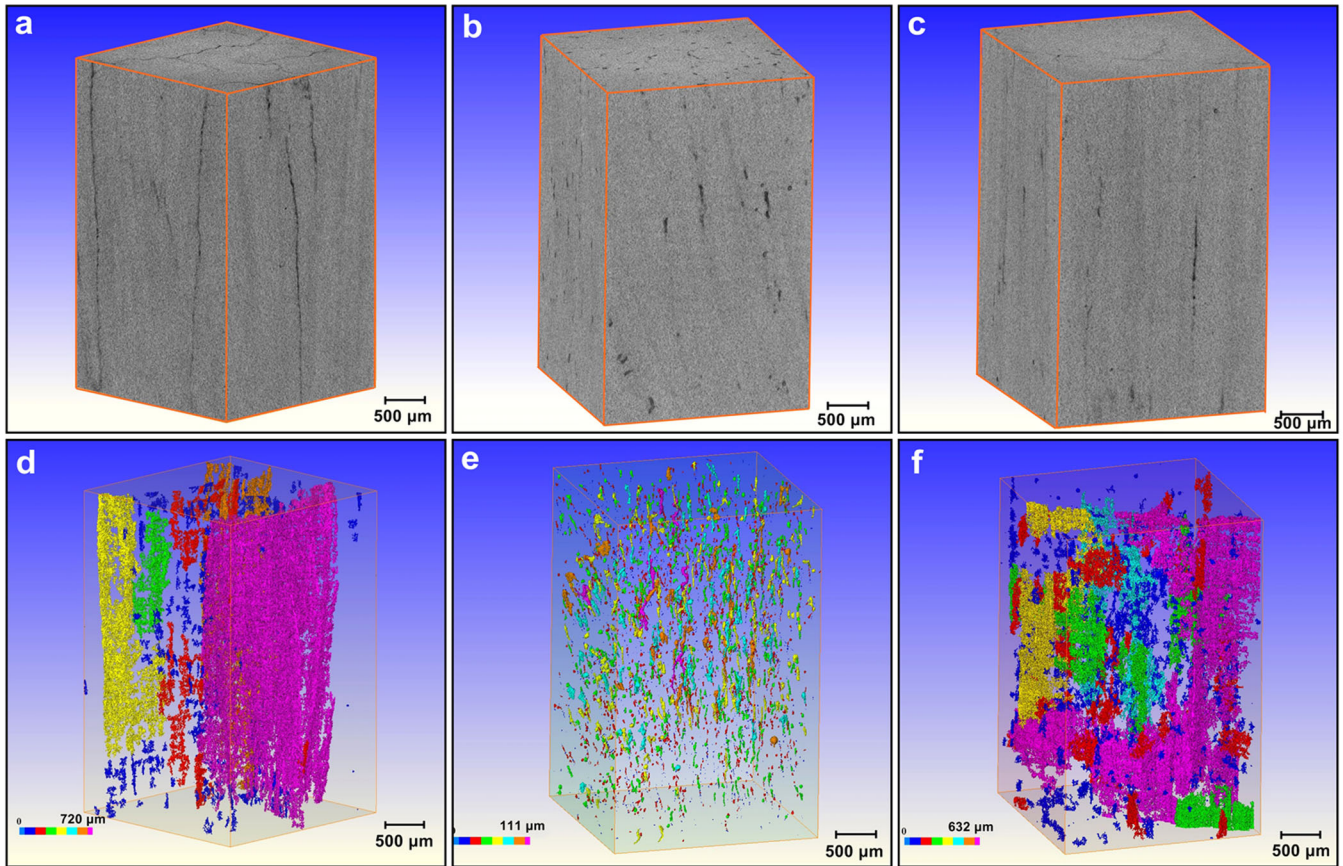
Fig. 2 XRT three-dimensional reconstruction images of different EBM NiTi alloys. a–c Corresponding to the reconstructed morphologies of S1, S5, and S7 respectively, **d–f** corresponding to defect distribution in the three-dimensional space of S1, S5 and S7 respectively.

whole fabrication process regardless of the change in electron beam current[28]. When the electron beam current is determined, the scanning rate of the electron beam increases, and the energy density decreases with the increase of SF[24], which means that proper energy input can only be generated when SF maintains an appropriate value, otherwise more defects will be formed. As shown in Fig. 2, S1 and S7 corresponding to a small and a large value of SF, respectively, present more defects, while S5 with a proper SF value shows fewer defects. Overall, S5 prepared with appropriate SF and FO of 70 mm s^{-1} and 15 mA by EBM actually possesses a denser structure.

Corrosion behavior of different EBM NiTi alloys

A large number of studies have shown that pores and cracks can significantly weaken the corrosion resistance of alloys[22,23]. Corrosive media can enter into the alloys through pores or cracks, thus it is easy to produce local acidification due to the relatively closed environment in the pores or cracks, accelerating the corrosion of alloys. Pores and cracks are also the most harmful defects in additive manufacturing alloys. Under the action of corrosive media and load, the alloys with pores or cracks are prone to stress corrosion cracking and corrosion fatigue, leading to material failure. Generally, the formation of pores and cracks needs to be strictly avoided for alloys or coatings used in corrosive media.

To reveal the corrosion behavior of EBM NiTi alloys with different fabrication parameters, electrochemical impedance spectroscopy (EIS) tests are conducted in 3.5 wt.% NaCl solution. The Bode frequency-impedance results (Fig. 3a) of EIS show that S5 has the highest impedance value in the low-frequency region among the different EBM NiTi alloys, which is almost equivalent to

the impedance value of the wrought NiTi alloy, while S1 has the lowest impedance value in the same frequency range. The impedance value in the low-frequency region usually reflects the protection of passive films, so it can be concluded that S5 and the wrought NiTi alloy have better corrosion resistance. In the high-frequency region, the impedance value reflects the solution resistance, and it can be seen that the impedance values of the four samples are all less than 10 Ω cm^2, which is consistent with the reports of literature indicating the high reliability of the test results[31]. Figure 3b shows the Bode frequency-phase angle plots of different NiTi alloys, it is apparent that S1 and S7 have two phase angle peaks thus containing two time constants. Both S5 and the wrought NiTi alloy show a broad phase angle peak in the same frequency range, which is usually generated by the superposition of at least two phase angle peaks thereby containing at least two time constants. The results of the Nyquist plot (Fig. 3c) show that S5 has a larger capacitive arc radius, followed by S7 and S1 in sequence. From the radius of the capacitive arc, it therefore follows that S5 has a better corrosion resistance than S7 and S1. The fitted EIS plots from the equivalent circuit as shown in the insert of Fig. 3a, where CPE$_{dl}$ and CPE$_f$ are constant phase elements of electric double layer and passive films, respectively, R_{ct} is the resistance of charge transfer, R_f is film resistance, R_s is solution resistance. The reliability of the equivalent circuit can be verified by the values of the electric double layer capacitance (C_{dl}), which can be calculated according to Brug's formula[32,33]:

$$C_{dl} = Q^{1/a}\left(R_s^{-1} + R_{ct}^{-1}\right)^{(a-1)/a} \tag{1}$$

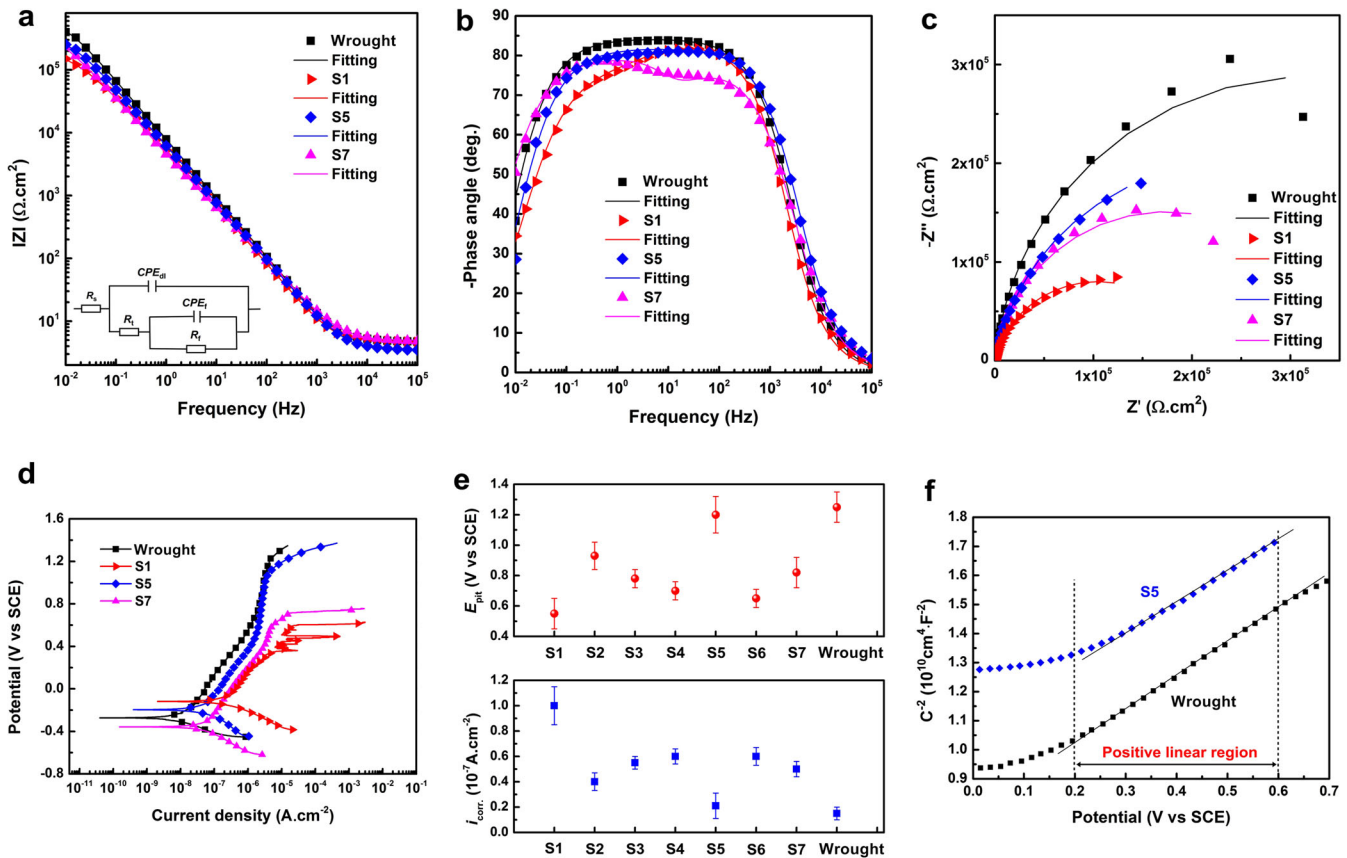$$C_{dl} = Q^{1/a}\left(\frac{R_s R_{ct}}{R_s + R_{ct}}\right)^{(1-a)/a} \tag{2}$$

Fig. 3 Electrochemical curves of EBM NiTi alloys with different fabrication parameters. a Frequency-impedance plots (the insert diagram referring to the equivalent circuit of EIS), **b** frequency-phase angle plots, **c** Nyquist plots, **d** potentiodynamic polarization plots of S1, S5, S7 and the wrought NiTi alloy, **e** distribution of E_{pit} and i_{corr} of different EBN NiTi alloys for six experiments, and **f** the Mott–Schottky curves of S5 and the wrought NiTi alloy.

Table 1. Electrochemical parameters obtained by fitting EIS curves for the wrought alloy, S1, S5, and S7.

Sample	R_s (Ω cm^2)	CPE$_{dl}$		R_t (Ω cm^2)	CPE$_f$		R_f (Ω cm^2)	χ^2
		Q_{dl} (Ω^{-1} s^{-a} cm^{-2}) a_0			Q_f (Ω^{-1} s^{-a} cm^{-2}) a			
The wrought	4.83	2.28×10^{-5}	0.937	6.35×10^{5}	2.37×10^{-6}	0.949	1.30×10^{6}	4.69×10^{-4}
S1	4.73	3.08×10^{-5}	0.929	1.46×10^{4}	1.21×10^{-5}	0.657	2.01×10^{5}	2.23×10^{-4}
S5	4.92	3.83×10^{-5}	0.873	3.16×10^{3}	3.99×10^{-6}	1.00	4.81×10^{5}	6.35×10^{-4}
S7	3.51	3.02×10^{-5}	0.910	1.21×10^{4}	1.23×10^{-6}	0.721	3.47×10^{5}	8.08×10^{-4}

where Q and a are the CPE_{dl} parameters. In most cases, the value of R_{ct} is much larger than that of Rs, so the aforementioned formula can be simplified as follows:

$$C_{dl} = Q^{1/a} R_s^{(1-a)/a} \qquad (3)$$

Using this formula, the C_{dl} values of different EBM NiTi alloys can be obtained based on the fitting results of Q, R_s, and a as shown in Table 1. The calculated values of C_{dl} for S1, S5, S7 and the wrought NiTi alloy are about 15.7, 11.0, 12.1, and 12.2 µF cm^{-2}, respectively, which are consistent with the C_{dl} values reported in the literature[34–36], indicating the reliability of the selected equivalent circuit. Additionally, the R_f values of different NiTi alloys indicate that S5 has a larger film resistance than S1 and S7, implying better corrosion resistance.

Figure 3e presents the potentiodynamic polarization plots of different EBM NiTi alloys in 3.5 wt.% NaCl solution. It is clear

that with the increase in alloy defects, the width of the passivation zone becomes narrow, the pitting potential (E_{pit}) decreases and the corrosion current density (i_{corr}) increases. Specifically, S5 and the wrought sample present the highest E_{pit} of 1.2 V$_{SCE}$, and S1 displays the lowest E_{pit} of 0.55 V$_{SCE}$. Meanwhile, the i_{corr} of S1, S5 and S7 are about 0.10 µF cm^{-2}, 0.02 µF cm^{-2} and 0.07 µF cm^{-2}, respectively, indicating that S5 has better corrosion resistance. It is worth noting that S5 exhibits almost the same corrosion resistance as the wrought NiTi alloy, although the former contains some porosity defects. Furthermore, the protection ability of passive films formed on the wrought sample and S5 is evaluated by Mott–Schottky plots (Mott–Schottky plots of S1 and S7 are shown in Supplementary Fig. 8). A positive linear zone from +0.2 V$_{SCE}$ to +0.6 V$_{SCE}$ is observed, indicating that the passive films formed on the wrought sample and S5 present a characteristic of n-type semiconductors. The carrier density (N_D) can be

calculated according to the equation as follows:

$$C^{-2} = \frac{2}{\varepsilon_r \varepsilon_0 e N_D} \left(E - E_{FB} - \frac{kT}{e} \right) \quad (4)$$

where C_{sc} is the space-charge capacitance, ε_r represents the dielectric of titanium oxide film, taken as 80 according to relevant literatures[37,38], ε_0 is the vacuum permittivity (8.845×10^{-14} F cm^{-1}), N_D and E are the carrier density in n-type passive films and the applied potential (V_{SCE}), respectively, e is the electron charge (1.6×10^{-19} C), and T is the absolute temperature, taken as 298 K. In addition, E_{FB} and k represent the flat-band potential (V_{SCE}) and Boltzmann constant (1.38×10^{-23} J K^{-1}), respectively. K_{slope} can be obtained by linear fitting the slope of the Mott-Schottky curve, and the value of N_D can be expressed as follows:

$$K_{slope} = \frac{dC^{-2}}{dE} = \frac{2}{\varepsilon_r \varepsilon_0 e N_D} \quad (5)$$

$$N_D = \frac{2}{\varepsilon_r \varepsilon_0 e} \left(\frac{dC^{-2}}{dE} \right)^{-1} \quad (6)$$

The linear fitting results of Mott–Schottky plots are shown in Table 2, where R^2 represents the level of linear fitting. The N_D values of the passive films formed on the wrought sample and S5 are 1.57×10^{20} cm^{-3} and 1.62×10^{20} cm^{-3}, respectively, which are significantly lower than those of passive films for stainless steels and aluminum alloys[39–42]. Generally, a low N_D value reflects the weak conductivity indicating good protection of passive films. Combining the results of EIS and potentiodynamic polarization as well as relevant reports, it can be established that the EBM NiTi alloys with proper fabrication parameters have better corrosion resistance than the NiTi alloys fabricated by vacuum plasma spraying[43], low-pressure plasma spraying[44], high velocity oxygen-fuel spraying[7,45], and laser-plasma hybrid spraying[46,47], displaying potential engineering application value. Therefore, the preparation of NiTi alloy by EBM can be a very promising engineering preparation technology.

In summary, the NiTi alloy with superior corrosion resistance is successfully fabricated by EBM, and the influence of fabrication parameters on the corrosion behavior of EBM NiTi alloys is investigated. Results indicate that the variation in fabrication parameters result in different defect types and defect number of NiTi alloys, thus, affecting the corrosion resistance. Excessive or insufficient SF and FO values can cause high susceptibility to defects during the fabrication process, especially in the formation of cracks, whereas there exist a few relatively uniformly-distributed pores in the EBM NiTi alloy when appropriate SF and FO values are selected. The alloys with the maximum cracks display the lowest corrosion resistance, whereas those with a few small pores uniformly distributed in the alloys possess superior corrosion resistance comparable to wrought NiTi alloys. The electrochemical results demonstrate that the EBM NiTi alloy with optimized fabrication parameters including SF of 70 mm s^{-1} and FO of 15 mA presents a higher E_{pit} and a lower i_{corr}, indicating good corrosion resistance. Meanwhile, a low carrier density of passive films equivalent to the wrought alloy is also displayed for the optimized EBM NiTi alloy, implying superior protection of passive films.

Table 2. Fitting parameters of Mott–Schottky plots and the calculated values of N_D for S5 and the wrought alloy.

Samples	K_{Slope} ($\times 10^{10}$)	N_D ($\times 10^{20}$ cm^{-3})	R^2
S5	10.9 ± 0.4	1.62 ± 0.15	0.985
The wrought	11.2 ± 0.3	1.57 ± 0.12	0.999

METHODS

Preparation of EBM NiTi alloys

NiTi alloy powder with equal atomic ratio was prepared by gas atomization. The EBM equipment with model Arcam A1 was used to prepare the NiTi bulk alloy with the size of 12 mm × 12 mm × 12 mm. EBM adopted a zigzag scanning path and rotated 90° between adjacent fabricating layers. The thickness of the powder layer was about 50 μm, the scanning rate was 1500 mm s^{-1} and the scanning distance was 0.2 mm. The acceleration voltage and the scanning current were 60 kV and 19 mA, respectively. Meanwhile, the preheating was operated before the fabrication process and the selected temperature of preheating for the bottom plate and the powder layer was 750 °C. Seven kinds of NiTi samples were fabricated using EBM by adjusting SF and FO parameters to reveal the influence of fabrication parameters on the corrosion resistance of NiTi alloy. The specific parameters of (SF, FO) for S1, S2, S3, S4, S5, S6, and S7 were (25 mm s^{-1}, 8 mA), (25 mm s^{-1}, 15 mA), (25 mm s^{-1}, 35 mA), (25 mm s^{-1}, 40 mA), (70 mm s^{-1}, 15 mA), (80 mm s^{-1}, 15 mA) and (100 mm s^{-1}, 15 mA), respectively.

Microstructure characterization

XRD (D/Max-2500PC) was used for phase analysis with radiation source of Cu Kα, and the scanning rate was 2° min^{-1}. To reduce the effect of rough surface on XRD tests, the same rough surface was kept by grinding with 400, 800, and 2000 grit silicon carbide sandpapers in sequence for different EBM NiTi alloy samples, and each XRD test was repeated twice to ensure the test accuracy. SEM (Maia 3) was used to characterize the morphology of EBM NiTi alloy. TEM (Tecnai G^2 F20) was used to further characterize the microstructure of EBM NiTi alloy, and the samples for TEM observation were prepared by the precision ion etcher with model RES 101. The defect distribution of different EBM NiTi alloys was measured by a three-dimensional XRT (Versa xrm-500) system with sub-micron resolution.

Electrochemical tests

The corrosion behavior of NiTi alloys with different EBM fabrication parameters in 3.5 wt.% NaCl solution (pH 6) was measured by Gamry 600+ electrochemical workstation. A traditional three-electrode cell (i.e., platinum sheet, saturated calomel electrode (SCE) and sample as the counter electrode, the reference electrode and the working electrode, respectively) was used for all electrochemical tests. EIS was conducted at open circuit potential (OCP), and the test frequency was from 100 kHz to 10 mHz. The OCP test with 3600 s was firstly carried out to get a stable potential before the EIS measurement. After the EIS tests, potentiodynamic polarization measurements were carried out at a scanning rate of 0.5 mV s^{-1} from −0.3 V versus OCP to +1.2 V versus SCE. Additionally, Mott-Schottky tests were operated to evaluate the protection capability of passive films with a scanning rate of 20 mV s^{-1} and a test frequency of 1000 Hz. Before the electrochemical tests, the EBM NiTi samples with the dimension of 10 mm (length) ×10 mm (width) ×4 mm (height) were sealed using epoxy resin with an exposed surface area of 1 cm^2, then the working surfaces were wet-ground with 400, 800, and 2000 grit silicon carbide sandpapers in sequence and thereafter polished using the diamond polish paste with 1.5 μm diameter. Each electrochemical test was repeated at least three times, and the results representing the average value were selected.

DATA AVAILABILITY

REFERENCES

1. Dutkiewicz, J. et al. Superelastic effect in NiTi alloys manufactured using electron beam and focused laser rapid manufacturing methods. *J. Mater. Eng. Perform.* **29**, 4463–4473 (2020).
2. Xiong, Z. et al. Selective laser melting of NiTi alloy with superior tensile property and shape memory effect. *J. Mater. Sci. Technol.* **35**, 2238–2242 (2019).
3. Chen, X. et al. The fabrication of NiTi shape memory alloy by selective laser melting: A review. *Rapid Prototyp. J.* **25**, 1421–1432 (2019).
4. Khoo, Z. X. et al. A review of selective laser melted NiTi shape memory alloy. *Materials* **11**, 1–14 (2018).
5. Elahinia, M. et al. Fabrication of NiTi through additive manufacturing: A review. *Prog. Mater. Sci.* **83**, 630–663 (2016).
6. Shi, Z. P. et al. Effect of Ni interlayer on cavitation erosion resistance of NiTi cladding by tungsten inert gas (TIG) surfacing process. *Acta Metall. Sin.* **33**, 415–424 (2020).
7. Crescenzo, C. D. et al. Ni–Ti shape memory alloy coatings for structural applications: optimization of HVOF spraying parameters. *Adv. Mater. Sci. Eng.* **2018**, 1–10 (2018).
8. Zeng, Z. et al. Wire and arc additive manufacturing of a Ni-rich NiTi shape memory alloy: Microstructure and mechanical properties. *Addit. Manuf.* **32**, 101151 (2020).
9. Ngo, T. D., Kashani, A., Imbalzano, G., Nguyen, K. T. Q. & Hui, D. Additive manufacturing (3D printing): A review of materials, methods, applications and challenges. *Compos. Part B-Eng.* **143**, 172–196 (2018).
10. DebRoy, T. et al. Additive manufacturing of metallic components—process, structure and properties. *Prog. Mater. Sci.* **92**, 112–224 (2018).
11. Frazier, W. E. Metal additive manufacturing: A review. *J. Mater. Eng. Perform.* **23**, 1917–1928 (2014).
12. Gu, D. D., Meiners, W., Wissenbach, K. & Poprawe, R. Laser additive manufacturing of metallic components: Materials, processes, and mechanisms. *Int. Mater. Rev.* **57**, 133–164 (2012).
13. Dai, N., Zhang, J., Chen, Y. & Zhang, L. C. Heat treatment degrading the corrosion resistance of selective laser melted Ti–6Al–4V alloy. *J. Electrochem. Soc.* **164**, C428–C434 (2017).
14. Dai, N. et al. Distinction in corrosion resistance of selective laser melted Ti–6Al–4V alloy on different planes. *Corros. Sci.* **111**, 703–710 (2016).
15. Dai, N., Zhang, L. C., Zhang, J., Chen, Q. & Wu, M. Corrosion behavior of selective laser melted Ti–6Al–4V alloy in NaCl solution. *Corros. Sci.* **102**, 484–489 (2016).
16. Qin, P. et al. Improved corrosion resistance on selective laser melting produced Ti-5Cu alloy after heat treatment. *ACS Biomater. Sci. Eng.* **4**, 2633–2642 (2018).
17. Ren, D. C. et al. Influence of manufacturing parameters on the properties of electron beam melted Ti-Ni alloy. *Acta Metall. Sin.* **56**, 1103–1112 (2020).
18. Gai, X. et al. In-situ monitoring of the electrochemical corrosion behavior in fluoride environment of cellular structured Ti6Al4V alloy fabricated by electron beam melting. *Corros. Sci.* **181**, 109258 (2021).
19. Gai, X. et al. In-situ monitoring of the electrochemical behavior of cellular structured biomedical Ti-6Al-4V alloy fabricated by electron beam melting in simulated physiological fluid. *Acta Biomater.* **106**, 387–395 (2020).
20. Zhou, L. et al. Morphological effects on the electrochemical dissolution behavior of forged and additive manufactured Ti–6Al–4V alloys in runway deicing fluid. *Surf. Coat. Tech.* **414**, 127096 (2021).
21. Bai, Y. et al. Improved corrosion behaviour of electron beam melted Ti–6Al–4V alloy in phosphate buffered saline. *Corros. Sci.* **123**, 289–296 (2017).
22. Zhang, L. M. et al. Influence of sealing treatment on the corrosion behavior of HVAF sprayed Al-based amorphous/nanocrystalline coating. *Surf. Coat. Tech.* **353**, 263–273 (2018).
23. Zhang, S. D., Wu, J., Qi, W. B. & Wang, J. Q. Effect of porosity defects on the long-term corrosion behaviour of Fe-based amorphous alloy coated mild steel. *Corros. Sci.* **110**, 57–70 (2016).
24. Wang, C., Tan, X., Liu, E. & Tor, S. B. Process parameter optimization and mechanical properties for additively manufactured stainless steel 316L parts by selective electron beam melting. *Mater. Des.* **147**, 157–166 (2018).
25. Wang, P., Sin, W. J., Nai, M. L. & Wei, J. Effects of processing parameters on surface roughness of additive manufactured Ti–6Al–4V via electron beam melting. *Materials* **10**, 1–11 (2017).
26. Pushilina, N. et al. Influence of manufacturing parameters on microstructure and hydrogen sorption behavior of electron beam melted titanium Ti–6Al–4V alloy. *Materials* **11**, 1–10 (2018).
27. Schwerdtfeger, J., Singer, R. E. & Koerner, C. In situ flaw detection by IR-imaging during electron beam melting. *Rapid Prototyp. J.* **18**, 259–263 (2012).
28. Cheng, B., Price, S., Lydon, J., Cooper, K. & Chou, K. On process temperature in powder-bed electron beam additive manufacturing: Model development and validation. *J. Manufact. Sci. Eng.* **136**, 061018 (2014).
29. Tan, L. & Crone, W. C. In situ TEM observation of two-step martensitic transformation in aged NiTi shape memory alloy. *Scr. Mater.* **50**, 819–823 (2004).
30. Gong, H. et al. Influence of defects on mechanical properties of Ti–6Al–4V components produced by selective laser melting and electron beam melting. *Mater. Des.* **86**, 545–554 (2015).
31. Zhang, L. M. et al. Understanding the roles of deformation-induced martensite of 304 stainless steel in different stages of cavitation erosion. *Tribol. Int.* **155**, 106752 (2021).
32. Brug, G. J., Vandeneeden, A. L. G., Sluytersrehbach, M. & Sluyters, J. H. The analysis of electron impedances complicated by the presence of a constant phase element. *J. Electroanal. Chem.* **176**, 275–295 (1984).
33. Hirschorn, B. et al. Determination of effective capacitance and film thickness from constant-phase-element parameters. *Electrochim. Acta* **55**, 6218–6227 (2010).
34. Zhang, L. M. et al. Significantly enhanced resistance to SRB corrosion via Fe-based amorphous coating designed with high dose corrosion-resistant and anti-bacterial elements. *Corros. Sci.* **164**, 108305 (2020).
35. Dec, W. et al. The effect of sulphate-reducing bacteria biofilm on passivity and development of pitting on 2205 duplex stainless steel. *Electrochim. Acta* **212**, 225–236 (2016).
36. Ismail, K. M., Jayaraman, A., Wood, T. K. & Earthman, J. C. The influence of bacteria on the passive film stability of 304 stainless steel. *Electrochim. Acta* **44**, 4685–4692 (1999).
37. Krawiec, H., Vignal, V., Schwarzenboeck, E. & Banas, J. Role of plastic deformation and microstructure in the micro-electrochemical behaviour of Ti-6Al–4V in sodium chloride solution. *Electrochim. Acta* **104**, 400–406 (2013).
38. Zakerin, N. & Morshed-Behbahani, K. Perspective on the passivity of Ti6Al4V alloy in H_2SO_4 and NaOH solutions. *J. Mol. Liq.* **333**, 115947 (2021).
39. Jayaraj, J., Shankar, A. R. & Mudali, U. K. Electrochemical and passive characterization of a beta type Ti45Zr38Al17 cast rod in nitric acid medium. *Electrochim. Acta* **85**, 210–219 (2012).
40. Levine, K. L., Tallman, D. E. & Bierwagen, G. R. Mott–Schottky analysis of aluminium oxide formed in the presence of different mediators on the surface of aluminium alloy 2024-T3. *J. Mater. Pro. Tech.* **199**, 321–326 (2008).
41. Gelderman, K., Lee, L. & Donne, S. W. Flat-band potential of a semiconductor: Using the Mott-Schottky equation. *J. Chem. Edu.* **84**, 685–688 (2007).
42. Zhang, L. M. et al. Thermally induced structure evolution on the corrosion behavior of Al–Ni–Y amorphous alloys. *Corros. Sci.* **144**, 172–183 (2018).
43. Cinca, N. et al. Structure characterization and wear performance of NiTi thermal sprayed coatings. *Smart Mater. Struct.* **19**, 085011 (2010).
44. Bitzer, M. Cavitation-resistant NiTi coatings produced by low-pressure plasma spraying (LPPS). *Wear* **328**, 369–377 (2015).
45. Verdian, M. M., Salehi, M. & Raeissi, K. Microstructure formation and properties of HVOF sprayed NiTi coatings prepared from amorphous/nanocrystalline NiTi powders. *Surf. Eng.* **26**, 491–496 (2010).
46. Hiraga, H., Inoue, T., Shimura, H. & Matsunawa, A. Cavitation erosion mechanism of NiTi coatings made by laser plasma hybrid spraying. *Wear* **231**, 272–278 (1999).
47. Hiraga, H. et al. Fabrication of NiTi intermetallic compound coating made by laser plasma hybrid spraying of mechanically alloyed powders. *Surf. Coat. Technol.* **139**, 93–100 (2001).

ACKNOWLEDGEMENTS

AUTHOR CONTRIBUTIONS

L.Z. and D.R.: Investigation, formal analysis, and writing – review and editing. H.J.: Conceptualization, writing – review and editing, and supervision. A.M. and E.D.: Formal analysis, and investigation. S.L. and W.J.: Sample preparation. Y.Z.: Conceptualization, supervision.

COMPETING INTERESTS

The authors declare no competing interests.

ADDITIONAL INFORMATION

Supplementary information The online version contains supplementary material available at https://doi.org/10.1038/s41529-022-00289-3.

Correspondence and requests for materials should be addressed to Haibin Ji or Yugui Zheng.

Reprints and permission information is available at http://www.nature.com/reprints

Publisher's note Springer Nature remains neutral with regard to jurisdictional claims in published maps and institutional affiliations.